Enhanced Z pinch using an externally applied magnetic field to stabilize the implosion of an aluminum plasma jet onto a coaxial wire

N. S. Edison, B. Etlicher, A. S. Chuvatin, and S. Attelan
Laboratoire de Physique des Milieux Ionises, Laboratoire du Centre National de la Recherche Scientifique, Ecole Polytechnique, 91128 Palaiseau, France

R. Aliaga
The Blackett Laboratory, Imperial College of Science, Technology and Medicine, London SW7 2BZ, United Kingdom
(Received 5 March 1993; revised manuscript received 12 July 1993)

We have performed Z-pinch experiments in which an aluminum plasma jet is imploded onto a coaxial, micrometer-diameter wire. X-ray pinhole images and temporally resolved x-ray data indicate that energy is initially supplied to the aluminum plasma jet, then transferred to the wire at the peak compression of the implosion. When a dc magnetic field is applied axially, growth of instabilities of the imploding aluminum plasma are reduced, and the production of x rays from the embedded wire is enhanced. These experiments demonstrate that an imploding plasma liner efficiently couples energy from a pulsed power generator into a micrometer-sized-diameter channel.

PACS number(s): 52.55.Ez, 52.80.Qj

I. INTRODUCTION

High-power discharges through micrometer-diameter wires or nonconducting fibers are actively being studied as a source of energetic x radiation or as a means of achieving thermonuclear fusion. Two-dimensional (2D) computer simulations [1] supported by experiments [2,3] have shown that the fiber undergoes surface ablation of a plasma which expands rapidly before recompressing. Instabilities arise during the recompression phase [4–7], which degrades the assembly of a uniform, high-density high-temperature plasma.

Alternatively, a large-diameter liner which implodes onto a coaxial fiber can support the rising current pulse. Large values of dI/dt may be attained by a staged energy transfer [8] without premature surface ablation and expansion of the fiber. Such staged implosions have been shown to be rather stable [9,10]. The pinch-on-wire (POW) configuration [11] is one method for producing a staged implosion. A preformed aluminum plasma jet with an embedded coaxial wire supports the rising current pulse and tempers coronal expansion from the target during the implosion. Previous studies show that instabilities associated with the wire alone are suppressed.

The focus of the present study is to combine the POW configuration with an axial magnetic field. In order to optimize the implosion conditions of the aluminum plasma, an axial magnetic field is applied externally. An aluminum plasma is injected into the field and evolves on a time scale long compared to that of the time required for the magnetic field to diffuse through the plasma. During the implosion the magnetic-field lines do not have time to diffuse through the plasma and are essentially frozen into place. This reduces the growth of instabilities and provides a more uniform pinch. If the applied field is small compared to the azimuthal field generated by the discharge, i.e., $B_z/B_\theta \ll 1$ throughout the implosion, the magnetic pressure of the axial field can be neglected, and the kinetic energy of the imploding ions is independent of the applied field. Thus, the final compression diameter should be unchanged but with a more uniform distribution of density and temperature along the pinch axis.

II. EXPERIMENTAL SETUP

These experiments were conducted on GAEL, a 2-Ω, 0.1-TW, 225-kA, 50-ns pulse line generator [12]. A pair of Helmholtz coils provide a dc magnetic field up to 300 G oriented parallel to the anode-cathode gap. The coils are wound 32 times around two 4-cm-diam spools separated by 2 cm and are energized by a standard 12-V car battery. The voltage drop across a load resistor monitors the current through the coil windings and, thus, determines the magnetic field.

The load consists of a 25-μm Cu wire with a mass-per-unit length of 45 μg/cm embedded in an aluminum plasma jet (see Fig. 1). The jet is prepared by exploding a 5-μm-thick Al foil which is collimated by a 3-mm-diam nozzle located in the anode. The plasma jet forms a Mach-2 plasma column between the discharge electrodes spaced 9 mm apart. The mass-per-unit length of the plasma column was approximately 15–30 μg/cm and was adjusted by varying the time delay between the foil explosion and the discharge of the generator [13]. Characteristics of the aluminum jet, jet-only implosions, time-dependent current, x-ray pulse, and streak data have been previously reported [14]. The shape of the aluminum plasma jet before the main current begins to flow can be seen in Fig. 2. A cone of plasma emerges from the anode with a divergence angle of $\approx 55°$, which places the jet velocity between Mach 1.7 and 2. The structure of the axis of the cone is due to the Cu wire and may be the interaction of the prepulse with plasma in the vicinity of the wire.

Diagnostics include a load-current monitor, a filtered

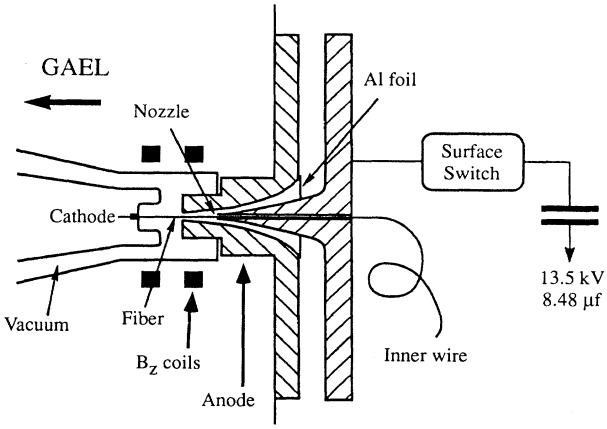

FIG. 1. Schematic of GAEL load region showing the electrodes, Cu wire, Al plasma jet nozzle, and Helmholtz coils.

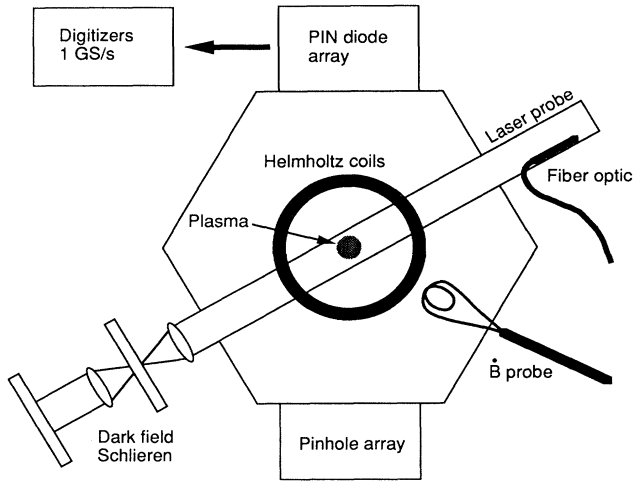

FIG. 3. View along the pinch axis of the arrangement of diagnostics and Helmholtz coils. GAEL is behind the pinch region in this diagram.

x-ray *p-i-n* diode array, time-resolved dark field schlieren photography, and a filtered time integrated pinhole camera array. Figure 3 shows the arrangement of the diagnostics around the load region. The *p-i-n* diode array consists of five pairs of Ross-matched, filtered diodes for determining the free-free and bound-free radiation spectrum for energies ranging from 2 to 10 keV (see Fig. 4). The diode signals have been calibrated such that their signal ratios can be considered accurate to within 5%. All diode signals as well as current and voltage traces were recorded by an Analytek digitizing system which can handle up to 24 channels at 500 MS/s or 12 channels at 1 GS/s on a single time base. Signals captured on different time bases are correlated by means of a laser fiducial generated by the schlieren probe. Thus, the temporal relations of all time-resolved data are known to within ±1 ns.

The schlieren photography used a pulsed dye laser operating at 5 896 Å with a 5-ns pulse width. After passing through the pinch region, 20- and 40-cm lenses focus and image the laser probe onto Polaroid type 667 film with a magnification of 2. A laser-line interference filter prevents light generated by the plasma from being recorded. A 200-μm wire placed at the focus of the 20-cm lens and parallel to the axis of the pinch blocks all

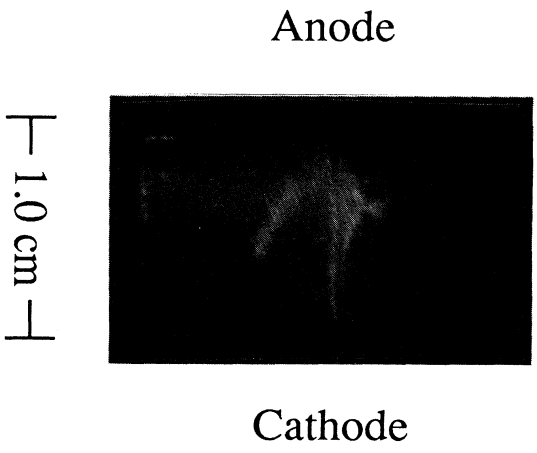

FIG. 2. Schlieren image taken just prior to the arrival of the main current pulse which shows the aluminum plasma jet and copper wire.

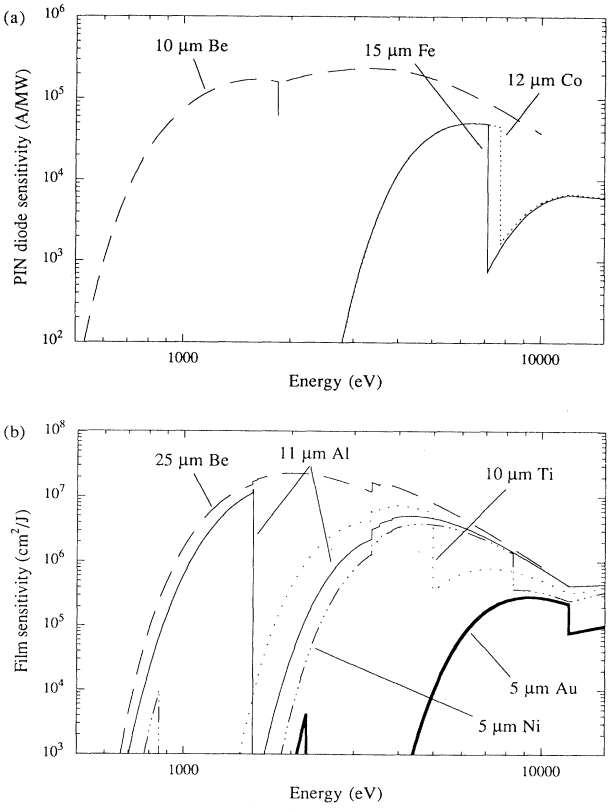

FIG. 4. Sensitivity curves for (a) *p-i-n* diode filter and (b) pinhole arrays. The sensitivities have been calculated using the XRD software.

rays that have been deflected by an angle of less than 2.5×10^{-4} radians [15]. Thus, light recorded on the film represents an average electron-density-gradient–length product of $\langle \nabla n_e L \rangle \geq 1.6\times10^{18}/\text{cm}^3$.

The pinhole camera array records nine images on SB-392 film and utilizes various filters and pinhole diameters to cover a broad range of energies (see Fig. 4). The choice of pinholes and filters is constrained by the limitations of the GAEL generator. Unfortunately, the present generator current does not produce enough x-ray flux to use pinholes smaller than 100 μm in diameter for hard filtering. We have recorded images with a 20-μm pinhole filtered by 10-μm aluminum, but these images are not suitable for reproduction.

III. RESULTS AND ANALYSIS

The conical initial plasma jet seen in Fig. 2 insures that the magnetic field compression will vary quadratically over the length of the pinch. Since the jet is created by a 3-mm-diam nozzle with a Mach-2 divergence the radii vary from 1.5 to 6.5 mm and the final axial field will vary by a factor of 20, assuming the final radius is the same over a length of 10 mm. For large applied axial fields, our requirement that $B_z/B_\theta \ll 1$ may no longer be justified along the entire length of the plasma column, especially near the cathode. If we permit $B_z/B_\theta < 10\%$, then this condition begins to break down at the cathode for $B_z \geq 200$ G. Here we have assumed a final plasma radius of 100 μm and 100 kA to give $B_\theta \approx 200$ T.

Figure 5 shows the timing between various signals of interest, the generator current, the load current, and a *p-i-n* diode channel. The current pulses begin with a 50-ns prepulse followed by the main pulse lasting about 60 ns. The load current has been integrated from a dB/dt probe and is assumed to be reliable only during the first 120 ns of the main discharge. In Fig. 6 the load current for various applied magnetic fields has been plotted. The difference of the ratios of the amplitudes of the prepulse compared to the main pulse is due to differences in the final inductance of the load. For low magnetic fields, instabilities increase the load inductance, which manifests itself as increased current losses.

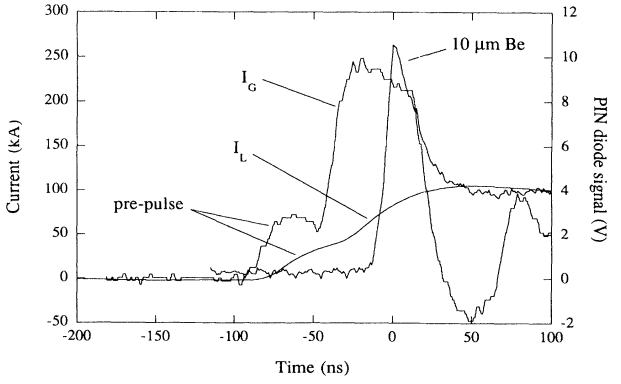

FIG. 5. Timing of the generator current (I_G), load current (I_L), and a *p-i-n* diode signal.

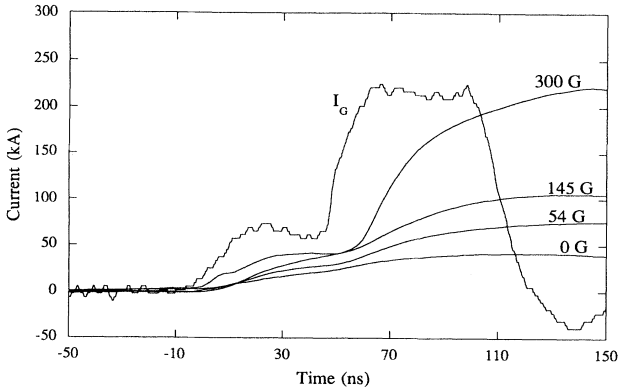

FIG. 6. Generator current (I_G) and current into the load for various applied magnetic fields.

Data from the *p-i-n* diodes can be seen in Figs. 7 and 8. The shot-to-shot variation is less than 25% for the x-ray data and is represented as an average value in Fig. 8. In Fig. 7 the peaks of the signals have been normalized to unity in order to compare the pulse characteristics of all channels. In the absence of an applied field, all x-ray pulses tend to follow similar temporal histories. For the

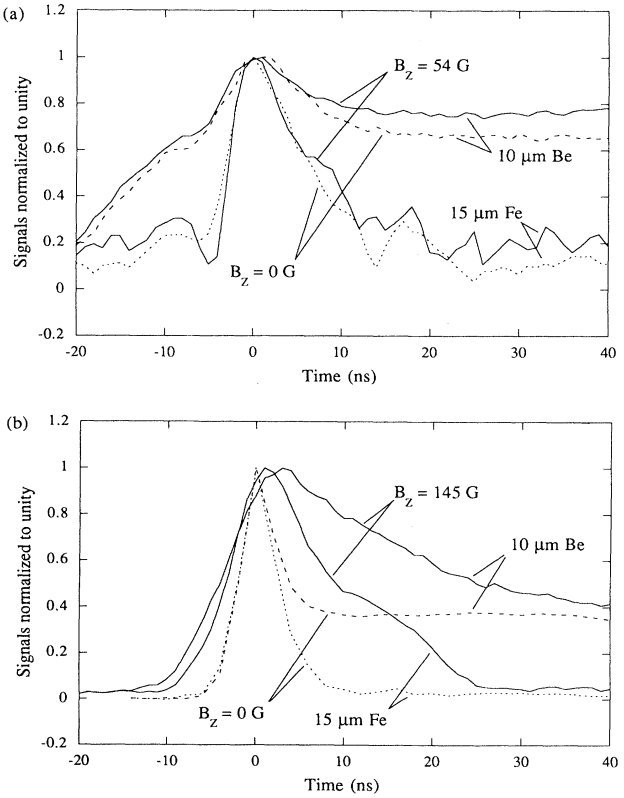

FIG. 7. X-ray pulses as measured by *p-i-n* diodes (a) for the aluminum plasma jet alone at $B_z = 0$ and 54 G and (b) for the POW configuration at $B_z = 0$ and 145 G.

aluminum jet alone [Fig. 7(a)], the softer x-ray channels encounter more radiation from the prepulse than the hard x-ray channels. As the magnetic field increases, the x-ray pulse widths become larger, with the lower-energy x-radiation pulses the most affected. This effect is seen in Fig. 8(a) where the x-ray pulse widths have been plotted for fields up to 300 G.

Figure 8 displays results taken from data such as that in Fig. 7, i.e., pulse widths and peak signals. The pulse widths in Fig. 8(a) show that the aluminum jet alone and POW configurations behave differently. Pulse widths for the POW configuration peak between 50 and 150 G, whereas the aluminum jet widths tend to increase with the applied field. However, both configurations look identical when the signals are rising. This indicates that radiation in the POW configuration is primarily due to the presence of a wire at the core of the implosion. Note that the hard x-radiation for some of the aluminum jet implosions is very weak, resulting in a large measurement error especially above fields of 100 G.

Another difference between the aluminum jet and POW configurations is in the magnetic field necessary to optimize x-ray emission. Figures 8(b) and 8(c) show the peak x-ray signals and x-ray yield as a function of the applied field. The x-ray yield is estimated by taking the product of the pulse width with the peak signal. Peak x-ray emission on all channels [Fig. 8(b)] occurs near 50 G for the aluminum jet alone. For the POW configuration the x-ray signals are always larger on a particular channel, and x-ray emission is maximum at about 150 G, with the hard channels being affected the most. The trend in peak x-ray emission carries over to the integrated x-ray yields [Fig. 8(c)]. The POW configuration consistently produces higher x-ray yields, with a maximum for 150 G, while the aluminum jet only is weakly optimized at 50 G.

Temperature information is also provided by the *p-i-n* diode array. Recall that the *p-i-n* diode signals scale almost identically in the absence of a magnetic field. This would suggest that the temperature is nearly constant throughout the implosion and that the radiating volume changes in time. The same effect is seen during compression for nonzero magnetic fields, but the difference in x-ray pulse widths shows that the plasma is cooling immediately after the peak of the compression, i.e., a higher proportion of soft to hard radiation.

In Fig. 9, the temperature at the peak compression of the pinches has been determined for various applied fields. The 5% accuracy in the diode signals gives temperatures to within 50%. Temperatures have been determined by comparing a theoretical spectrum with one calculated from the diode data assuming no line emission between 5 and 8.5 keV. Using various filters to scan the spectrum, we have verified by the absorbant method that

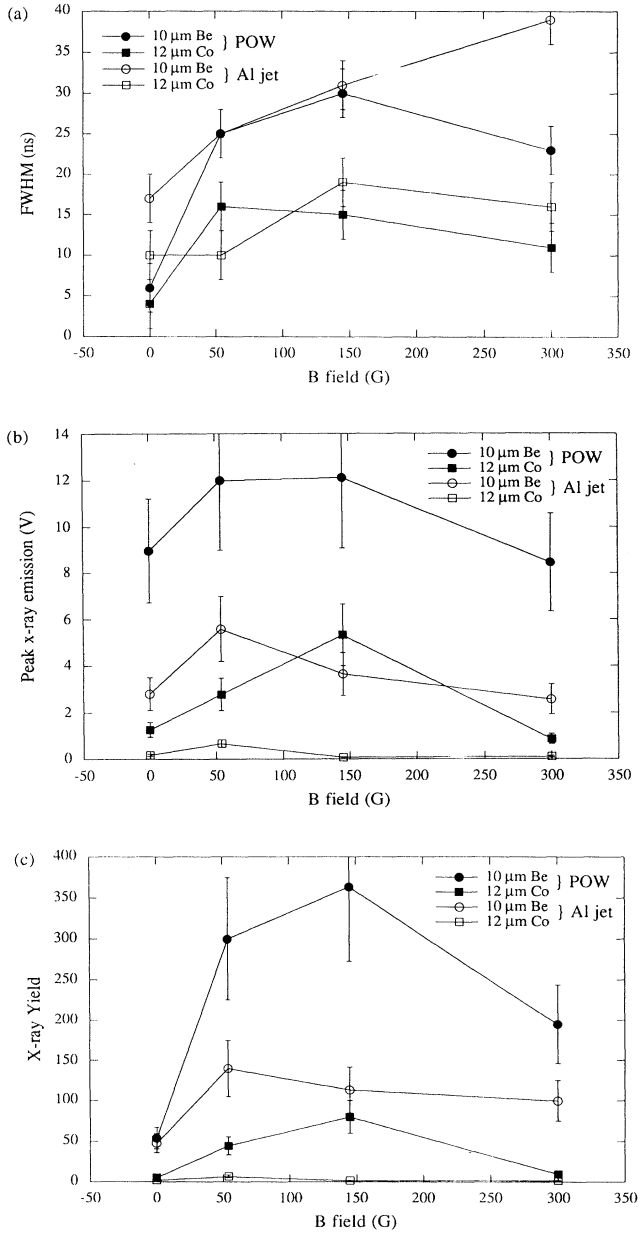

FIG. 8. Reduction of *p-i-n* diode data for various applied magnetic fields: (a) x-ray pulse widths, (b) peak x-ray emission, (c) x-ray yields.

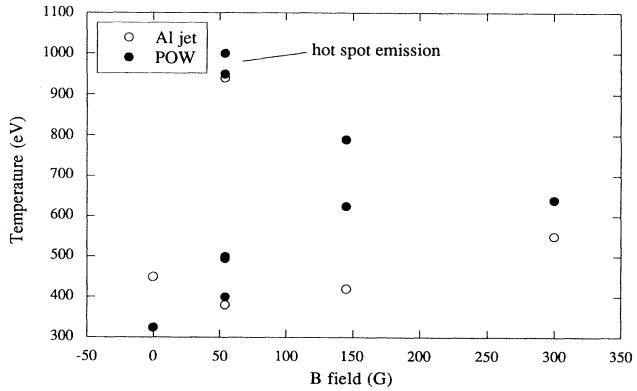

FIG. 9. Temperature at the peak of the compression as a function of applied magnetic field.

the line emission in this region is negligible compared to the continuum. However, using soft Ross pairs below 5 keV and the absorbant method strongly implies that line emission dominates over the continuum radiation. Line radiation above 8.5 keV can be ignored by proper selection of filters, i.e., filters with absorption edges below 8.5 keV.

The data at 50 G above 900 eV is assumed to be from hot spots associated with poorly stabilized compressions. The aluminum-jet-only data at this point is inconclusive. Data at zero applied fields tend to be dominated by emission from hot instabilities (see also pinhole data, Fig. 11). At 300 G radiation is dominated by bremsstrahlung emission due to the electron-beam interaction with the anode and poor compression. This is to be expected since the basic assumption, $B_z \ll B_\theta$, begins to break down near the cathode. Even the results at 50 and 150 G may show a false trend due to measurement errors. However, data for the POW configuration appear to be much better. The temperature tends to rise with increasing field strength up to 150 G, then trail off. Similarly, this makes sense when considering the optimization of peak x-ray emission at 150 G (Fig. 8). One would expect to see more radiation (and of a harder kind) for a plasma with a higher temperature.

Figure 10 shows the results of the schlieren photography. The temporal information associated with each subfigure is determined with respect to the peak in the x-ray yield as given by the *p-i-n* diode signals. The aluminum jet alone appears in Figs. 10(a) and 10(b). Figure 10(a) was taken early in the implosion and zippering is evident from the cathode to about the center of the liner. The POW configuration data is shown in Figs. 10(c)–10(h). In these subfigures the Cu wire has vaporized and stabilized the center of the liner. Before and up to the time of peak compression, the imploding jet displays a large amount of structure. However, after the peak of the implosion the liner is cylindrically symmetric and much more homogeneous along the pinch axis, as seen in Figs. 10(e), 10(g), and 10(h).

The schlieren images in Figs. 10(e), 10(g), and 10(h) clearly show the remnants of the Cu wire on the pinch axis several nanoseconds after the peak of the implosion. Even though the entire wire has been vaporized and ionized, the original geometry remains essentially intact throughout the implosion, with a maximum radial expansion of 200 μm. This give a volume expansion factor of about 100, which implies that the density has dropped to approximately $10^{21}/\text{cm}^3$ from solid density.

Figure 11 is a composite of eight shots from the pinhole-camera array for various applied magnetic fields on both pinch configurations. Figures 11(a)–11(d) show the aluminum plasma jet alone, and Figs. 11(e)–11(h) display the POW configuration. Each subfigure contains up to five time-integrated images of the pinch (see Fig. 4 and Table I for a list of filters, thicknesses, absorption edge energies and pinhole diameters). Fewer images are shown for the aluminum jet only since no data were recorded on the hardest channels.

In order to get an idea of the temporal history of the implosions, one should correlate the x-ray diode data (see Fig. 7) with the pinhole data. The diode signals give an approximate integration time for the pinhole data, as well as indicate the occurrences of hot-spot formation within the pinch. Additionally, since the x-ray signal widths depend on the hardness of the filters, one could, in principle, derive a temporal resolution based on the pinhole images alone.

For the aluminum jet configuration, increasing the applied field reduces the growth rate of all instabilities, most notably for $m=1$ and higher-order instabilities. This effect can be seen in Figs. 11(a)–11(d). At magnetic fields less than 60 G, $m=1$-instabilities are readily apparent. However, as the field is raised from 0 to 54 G, the magnitude of the "kinks" decreases and the plasma becomes more cylindrically symmetric. Above fields of 140 G, $m=1$ instabilities are negligible compared to $m=0$- instabilities. In addition, the axial homogeneity of the aluminum plasma at the peak of the implosion tends to increase with the axial field. The spatial frequency of $m=0$ instabilities is reduced, producing larger regions of homogeneous plasma. For a field of 300 G, the effects of both $m=0$ and $m=1$-instabilities are nearly absent, giving a plasma liner with radiating regions of homogeneity greater than 3 mm along the pinch axis, as seen in Fig. 11(d).

Radiation from the aluminum jet is seen only on channels $A-C$, which gives a maximum energy of 5 keV. For

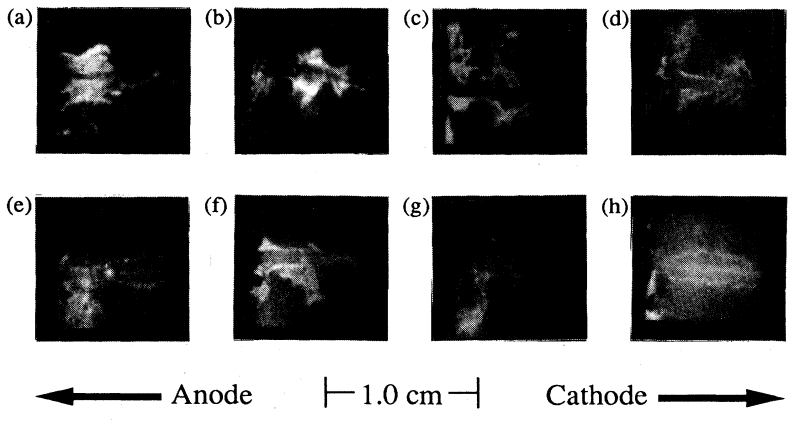

FIG. 10. Time-resolved schlieren images for various axial magnetic fields for the aluminum plasma jet only at (a) 0 G, $t=-15$ ns and (b) 145 G, $t=-10$ ns; for the POW configuration (c) 0 G, $t=-10$ ns; (d) 54 G, -5 ns; (e) 54 G, $t=10$ ns; (f) 145 G, $t=0$ ns; (g) 145 G, $t=10$ ns; and (h) 300 G, $t=20$ ns.

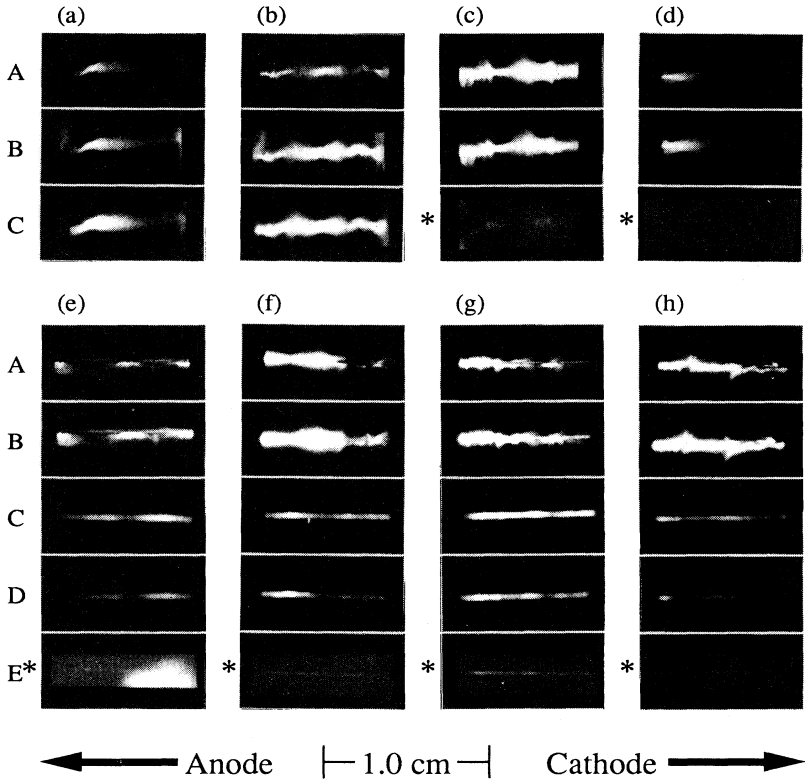

FIG. 11. Time-integrated data from the pinhole-camera array (see Table I for filter and pinhole information) for various axial magnetic fields for the aluminum plasma jet only : (a) 0 G, (b) 54 G, (c) 145 G, (d) 300 G; and for the POW configuration: (e) 0 G, (f) 54 G, (g) 145 G, (h) 300 G. An asterisk indicates that the subfigure has been printed so as to improve the contrast.

applied fields greater than 140 G, radiation is very weak on channel *C* (Ni) while the images for channel *A* (Be) have become brighter than those on channels *B* (Al). This indicates that the temperature is lower and not capable of producing a significant amount of radiation above 2 keV. The increase in the proportion of broadband radiation (channel *A*) to radiation below 1.5 keV (channel *B*) as well as the decrease in peak x-ray emission (Fig. 8) suggests that the pinch is emitting primarily in the uv and xuv spectra for long periods of time, i.e., greater than 30 ns.

For the POW configuration, data consistently appear on channels *A* – *E*. Channel *E* is, in general, too weak to be seen in these figures, and the printing has been enhanced so as to improve the contrast. Channels *C*, *D*, and *E* show emission from the wire only, whereas, on the other channels, both the copper wire and aluminum plasma are present. The images from channels *D* and *E* require radiation of at least 6 keV. X rays this energetic can only have been produced by the excitation of the *K* shell of copper.

TABLE I. Filter thicknesses, pinhole diameters, and cutoff energies used for time-integrated pinhole-array camera data. Channel labels correspond to the labeling of data in Fig. 11.

Channel labels	Filter material	Pinhole diameter (μm)	Thickness (μm)	Absorption edge (keV)
A	Be	50	25	0.11
B	Al	100	11	1.56
C	Ni	200	5	8.33
D	Ti	200	10	4.97
E	Au	100	5	11.9

The pinhole images show that the wire maintains its shape during peak emission from the pinch. Data from a 20-μm pinhole reveal that the wire has not expanded by more than a factor of 10 during the compression. Channel *A* also indicates that the wire has remained intact. However, this channel is complicated by the presence of emission from the aluminum plasma. Other images exhibit penumbral blurring due to pinhole diameters several times larger than that of the wire. The pinhole data are in agreement with the schlieren data. Figs. 10(e), 10(g), and 10(h), which imply that the wire vaporizes at the time of maximum compression.

IV. CONCLUSIONS

The differences in the radiative emission from our pinch loads is definitely due to the presence of the copper wire at the center of the implosion. Load current and pinhole data imply that energy is efficiently coupled into the wire at the peak compression of the implosion. Kinetic energy from the imploding shell plasma heats, vaporizes, and ionizes the wire to a temperature of several hundred eV. In addition, during stagnation, the load current may be switched into the wire to provide additional Joule heating. The fact that the wire does not chaotically explode suggests that most of the load current initially flows through the outer shell plasma. This is to be expected since the resistance of the aluminum jet plas-

ma is much lower than that of the wire.

Optimization of peak x-ray emission and integrated x-ray yields is due to the reduced growth of instabilities and improved axial homogeneity of the imploding shell. The difference in the applied field strengths required to optimize x-ray emission from each of our load configurations is at present not understood. Perhaps the magnetic field required to optimize the x-ray emission is related to the total mass at the peak of the compression. Then the mass difference between the two configurations would account for the different optimization fields observed in Fig. 8.

Further optimization of the peak x-ray emission may be possible by performing a more detailed study in the vicinity of 50 G for the aluminum plasma jet alone or 150 G for the POW configuration, as suggested by Fig. 8. In addition, we are redesigning our Al plasma jet nozzle to achieve higher Mach numbers in order to improve uniformity of the imploding plasma along the pinch axis.

Final compression is relatively independent of the applied magnetic field, which can be seen in Fig. 11 panels *A*. The radius of the radiating region is about 1 mm for all magnetic field strengths, especially near the anode where the magnetic field is compressed the least. At an initial field of 300 G and a radius of 6.5 mm, the magnetic field near the cathode may compress to about 30 T, which is comparable to a B_θ of 200 T. At such field strengths, the effects of the magnetic pressure cannot be ignored in the implosion, and the kinetic energy of the aluminum ions is reduced. This explains the decrease in compression from the anode region to the cathode region in Fig. 11(d).

Comparison of the pinhole images for the two load configurations reveals significant differences in the resulting implosions. The POW configuration produces harder radiation as evidenced by the presence (or lack thereof in the aluminum jet case) of x radiation above 6 keV. Channel *C* consistently radiates as a wire source in the POW configuration, but emits strongly in the aluminum jet case only for the fields studied below 60 G. The absence of emission from the aluminum plasma shell in the POW configuration reveals that the collision with the wire core cools the outer plasma shell. The collision efficiently transfers the kinetic energy of the imploding aluminum ions to the copper wire resulting in a hot dense core plasma surrounded by a cooler plasma shell. The harder x radiation from the wire implies that the wire is much hotter than the aluminum plasma shell. As the outer plasma shell cools, its resistance rises rapidly, in contrast to the falling resistance of the core. The above process provides a means for transferring the load current into the wire.

Comparison of the behavior of the Al plasma jet with and without the copper wire suggests that the dynamics of the implosion is independent of the presence of the wire. This is indicated by both the schlieren and the pinhole data (Figs. 10 and 11). Cylindrical symmetry of the aluminum plasma pinch is enhanced in both load configurations as the axial field increases. We have observed that the current rise in the load does not depend on the presence of the copper wire, at least prior to the time of maximum compression. Thus, optimization and development of the plasma jet can be done separately from the POW configuration.

In summary, we have observed an increase in x-ray emission moving to higher energy as the magnetic field increases with an optimum yield at 50 G for the aluminum plasma jet alone and at 150 G for the POW configuration. The addition of an axial magnetic field reduces the growth of instabilities associated with *Z* pinches and produces a more homogeneous plasma on the pinch axis. The implosion of the aluminum plasma jet appears unaffected by the presence of a wire at its core. Furthermore, a dense plasma ($n_e \approx 10^{21}/\text{cm}^3$) in the original shape of the wire remains at the core of the implosion after the main current pulse has begun to subside. Densities of this magnitude in conjunction with the axial uniformity provided by the POW configuration have applications for x-ray lasers and thermonuclear fusion.

ACKNOWLEDGMENTS

Special thanks are given to Pascal Zehnter and Claude Rouille for their experimental assistance, and Rick Spielman for generously supplying the x-ray-detector software. This work was supported by ETCA/CEG under Contact No. 420/115/01.

[1.] I. R. Lindemuth, F. H. McCall, and R. A. Nebel, Phys. Rev. Lett. **62**, 264 (1989).

[2] J. D. Sethian, A. E. Robson, K. A. Gerber, and A. W. DeSilva, Phys. Rev. Lett. **59**, 892 (1987).

[3] J. E. Hammel and D. W. Scudder, in *Proceedings of the Fourteenth European Conference on Controlled Fusion and Plasma Physics,* edited by F. Engelmann and J. L. Alvarez Rivas (European Physical Society, Petit-Lancy, Switzerland, 1987), Pt. 2, p. 450.

[4] C. Stalling, K. Nielsen, and R. Schneider, Appl. Phys. Lett. **29**, 404 (1976).

[5] S. M. Zakharov, G. V. Ivanankov, A. A. Kolomenskii, S. A. Pikuz, and A. I. Samokhin, Fiz. Plazmy **9**, 469 (1983) [Sov. J. Plasma Phys. **9**, 271 (1983)].

[6] L. E. Aranchuk, S. L. Bogolyubskii, G. S. Volkov, V. D. Korolev, Yu. V. Koba, V. I. Liksonov, A. A. Lukin, L. B. Nikandrov, O. V. Telkovskaya, M. V. Tulupov, A. S. Chernenko, V. Ya. Tsarfin, and V. V. Yankov, Fiz. Plazmy **12**, 1324 (1986) [Sov. J. Plasma Phys. **12**, 765 (1986)].

[7] E. S. Figura, G. H. McCall, and A. E. Dangor, Phys. Fluids B **3**, 2835 (1991).

[8] V. P. Smirnov, Plasma Phys. Controlled Fusion **33**, 1697 (1991).

[9] R. B. Spielman, M. K. Matzen, M. A. Palmer, P. B. Rand, T. W. Hussey, and D. H. McDaniel, Appl. Phys. Lett. **47**, 229 (1985).

[10] H. U. Rahman, P. Ney, F. J. Wessel, A. Fisher, and N.

Rostoker, in *Dense Z-Pinches,* edited by N. Pereira, J. Davis, and N. Rostoker, AIP Conf. Proc. No. 195 (AIP, New York, 1989), p. 351.

[11] F. J. Wessel, B. Etlicher, and P. Choi, Phys. Rev. Lett. **69**, 3181 (1992).

[12] J. Delvaux, H. Lamain, C. Rouille, H. J. Doucet, J. M. Buzzi, M. Gazaix, and B. Etlicher, in *Proceedings of the Fourth International Topical Conference on High Power Electron and Ion Beam Research and Technology, Palaiseau, 1981,* edited by H. J. Doucet and J. M. Buzzi (Ecole Polytechnique, Palaiseau, France, 1981), Vol. 2, p. 775.

[13] M. Gazaix, H. J. Doucet, B. Etlicher, J. P. Furtlehner, H. Lamain, and C. Rouille, J. Appl. Phys. **56**, 3209 (1984).

[14] P. Audebert, H. Lamain, B. Dufour, C. Rouille, B. Etlicher, L. Voisin, and P. Romary, in *Proceedings of the Eighth International Conference on High Power Particle Beams, Novosibirsk, 1990,* edited by B. Brelzman and B. Knyazev (World Scientific, Singapore, 1990), Vol. 1, p. 422.

[15] *Methods of Experimental Physics: Plasma Physics, Part B,* edited by R. H. Lovberg and H. R. Griem (Academic, New York, 1971), p. 22.

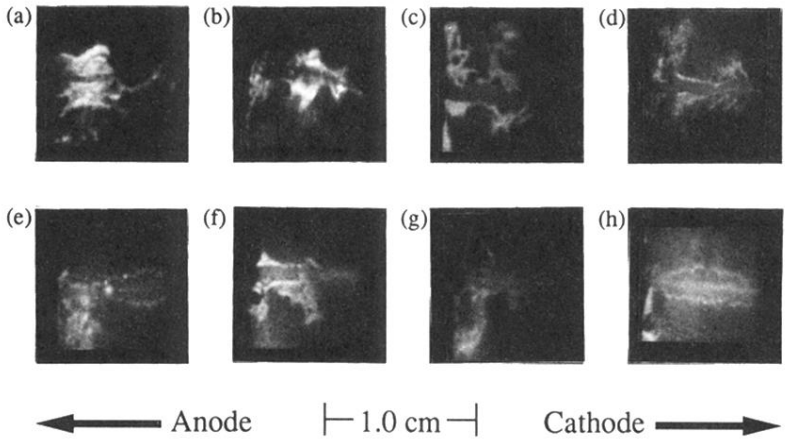

FIG. 10. Time-resolved schlieren images for various axial magnetic fields for the aluminum plasma jet only at (a) 0 G, $t=-15$ ns and (b) 145 G, $t=-10$ ns; for the POW configuration (c) 0 G, $t=-10$ ns; (d) 54 G, -5 ns; (e) 54 G, $t=10$ ns; (f) 145 G, $t=0$ ns; (g) 145 G, $t=10$ ns; and (h) 300 G, $t=20$ ns.

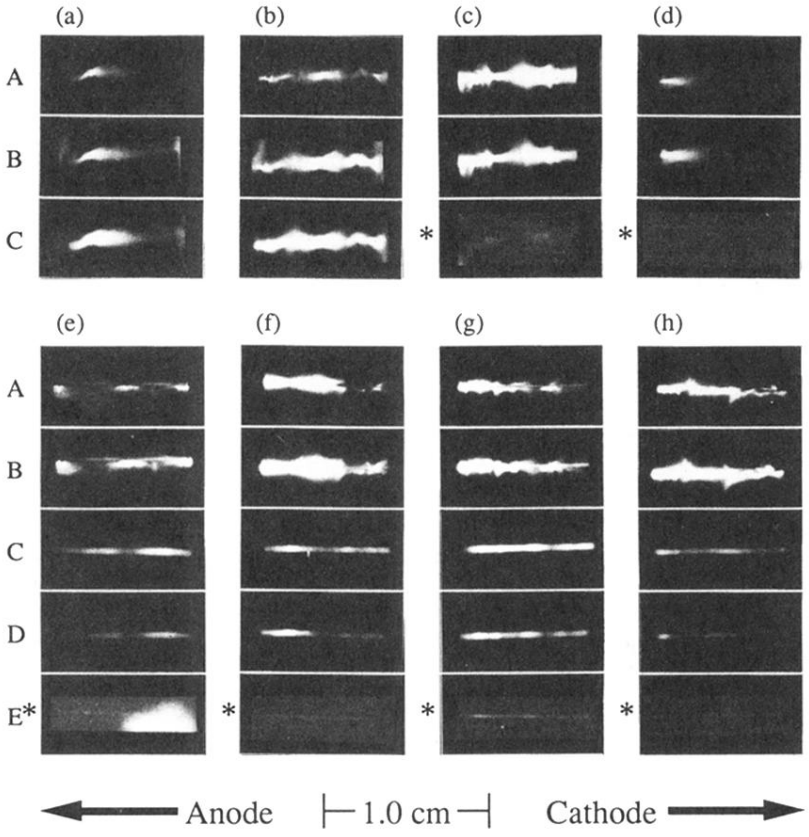

FIG. 11. Time-integrated data from the pinhole-camera array (see Table I for filter and pinhole information) for various axial magnetic fields for the aluminum plasma jet only : (a) 0 G, (b) 54 G, (c) 145 G, (d) 300 G; and for the POW configuration: (e) 0 G, (f) 54 G, (g) 145 G, (h) 300 G. An asterisk indicates that the subfigure has been printed so as to improve the contrast.

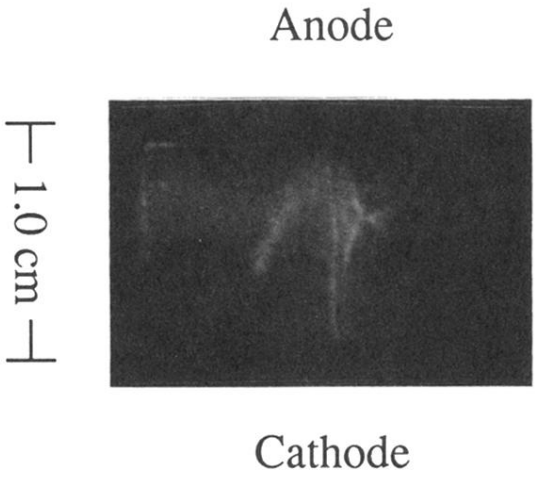

FIG. 2. Schlieren image taken just prior to the arrival of the main current pulse which shows the aluminum plasma jet and copper wire.